## PAPER

Check for updates

# Customized $CO_2$ electroreduction to methane or ethylene by manipulating *H and *CO adsorption on Cu/CeO$_x$ catalysts†

Tinghui Yang, Yingbing Zhang, Zichao Huang, Jianping Yang [ID] * and Min Kuang [ID] *

The coverage of *CO and *H intermediates on the surface of a catalyst plays a pivotal role in determining the selectivity towards $C_1$ or $C_2$ products in the electrochemical $CO_2$ reduction reaction ($CO_2$RR). In this study, we engineered two types of interfaces involving copper and rare earth metal oxides, specifically Cu/CeO$_x$ and Cu/CuCeO$_x$ solid solution, which exhibit enhanced binding affinities for *H and *CO adsorbates in the $CO_2$RR, respectively. As a result, the Cu/CuCeO$_x$ catalyst delivered an ethylene faradaic efficiency of 40.2% at a partial current density of $-245.7$ mA cm$^{-2}$, whereas the Cu/CeO$_x$ catalyst presented a methane faradaic efficiency of 38.6% at a partial current density of $-198.3$ mA cm$^{-2}$. Results of theoretical and experimental analyses have demonstrated that the Cu–Ce–O$_x$ solid solution markedly enhances *CO adsorption by stabilizing Cu$^+$ species, thereby favoring its dimerization to ethylene rather than converting to methane through hydrogenation. This investigation elucidates a strategy for directing the selective electroproduction of $C_1$ or $C_2$ compounds from the $CO_2$RR by effectively manipulating *H and *CO adsorption on Cu/CeO$_x$ catalysts.

## Introduction

The relentless rise in atmospheric $CO_2$ levels, predominantly driven by anthropogenic activities, has been identified as a principal factor exacerbating global warming, eliciting widespread concern across the globe.[1,2] Within this critical context,

*State Key Laboratory for Modification of Chemical Fibers and Polymer Materials, College of Materials Science and Engineering, Donghua University, Shanghai 201620, China. E-mail: jianpingyang@dhu.edu.cn; mkuang@dhu.edu.cn*

† Electronic supplementary information (ESI) available. See DOI: https://doi.org/10.1039/d4ta01808g

*Min Kuang is currently a professor in the College of Materials Science and Engineering at Donghua University, China. She received her PhD from the Laboratory of Advanced Materials at Fudan University. Following this, she joined the School of Materials Science and Engineering at Nanyang Technological University as a postdoctoral research associate. Her research focuses on developing advanced electrochemical $C_1$-to-fuel conversion systems and exploring efficient electrocatalysts.*

**Min Kuang**

the electrochemical carbon dioxide reduction ($CO_2$RR), especially when powered by renewable energy sources like solar and wind, has emerged as a vital strategy for carbon balance restoration.[3–5] Distinct from the generation of simpler $C_1$ products like formic acid (HCOOH) and carbon monoxide (CO),[6] there is an intensified demand for the production of high energy density hydrocarbons, notably methane ($CH_4$) and ethylene ($C_2H_4$), which are envisioned as potential sustainable fuels.[7–9] To date, copper-based materials, endowed with optimal adsorption energy for the *CO intermediate, have been heralded as the most effective catalysts for facilitating the conversion of $CO_2$ into valuable hydrocarbons.[10,11] In pursuit of this, a spectrum of Cu-based electrocatalysts, encompassing metallic Cu, Cu oxides,[12–14] Cu-integrated metal–organic frameworks (MOFs),[15,16] and Cu-centric molecules,[17,18] have been meticulously developed, marking significant strides in the electrocatalytic conversion of $CO_2$ to $CH_4$ or $C_2H_4$. Nevertheless, the design of cost-effective and durable catalysts tailored for the targeted transformation of $CO_2$ into high-energy products continues to pose a formidable challenge.

The mechanism underlying the $CO_2$RR involves the initial reduction of $CO_2$ to adsorbed *CO, succeeded by *CO hydrogenation and/or C–C coupling processes.[8,19] Recent investigations have illuminated that *CO hydrogenation to *CHO represents the rate-limiting step in $CH_4$ generation, while *CHO also acts as a pivotal intermediate for multi-carbon ($C_2$) products.[4,20] Moreover, the journey from *CO to hydrocarbons encapsulates a multi-step hydrogenation sequence, with *H emerging as a crucial intermediary for hydrocarbon synthesis.

Consequently, fine-tuning the adsorption dynamics of *CO and *H presents a promising avenue for steering the $CO_2RR$ towards desired products, particularly for $CH_4$ and $C_2H_4$. For example, Zheng et al. showcased that the strategic incorporation of two metal dopants, Zn and Mn, into Cu matrices could simultaneously modulate the coverage of *H and *CO, enabling the fine-tuning of selectivity between $CH_4$ and $C_2H_4$.[21] Similarly, Sargent et al. effectively manipulated *CO coverage through varying $CO_2$ concentrations, achieving tunable product specificity from $C_2H_4$ to $CH_4$.[22] In a parallel vein, Wei and colleagues enhanced the adsorption of the CO intermediate by augmenting polyaniline on Cu substrates, thereby activating $CO_2$ molecules and yielding a significant faradaic efficiency (FE) for $C_2$ products.[23] Despite these advances, attaining high selectivity shifts between desired products using analogous materials remains elusive, thereby underscoring the impetus for novel catalyst development.

In this report, we introduce an innovative strategy employing functional rare-earth metal oxides to facilitate selectivity switching between $CH_4$ and $C_2H_4$ products by modulating *H and *CO adsorption (Fig. 1). Two distinct electrocatalysts, Cu/$CeO_x$ and a Cu/$CuCeO_x$ solid solution ($0 < X < 2$), were synthesized, with the $CeO_x$ component enhancing *H coverage through expedited water dissociation, while $Cu–Ce–O_x$ solid solutions stabilize $Cu^+$ species, augmenting *CO adsorption and catalyzing the C–C coupling process. Electrochemical $CO_2RR$ evaluations revealed that the Cu/$CuCeO_x$ catalyst achieved an ethylene FE of 40.2% at a partial current density of $-245.7$ mA cm$^{-2}$, in contrast to the Cu/$CeO_x$ variant, which exhibited a methane FE of 38.6% at a partial current density of $-198.3$ mA cm$^{-2}$. Density functional theory (DFT) calculations further illustrated that $Cu–Ce–O_x$ solid solutions significantly reduce the formation energy of the *COCHO intermediate, thereby enhancing $C_2H_4$ production. This paradigm of adjusting $CO_2RR$ selectivity via intermediary coverage heralds new avenues for designing innovative Cu-based nanocomposite catalysts.

## Results and discussion

The Cu/$CuCeO_x$ catalyst was synthesized utilizing the coprecipitation methodology delineated in previous studies,[24] and subsequently subjected to annealing in a mixed atmosphere of 5 vol% $H_2$/Ar (Fig. 2a and S1†). In contrast, the Cu/$CeO_x$ catalyst was fabricated through a bifurcated procedure: initially, $CeO_x$ was prepared devoid of any Cu precursor via
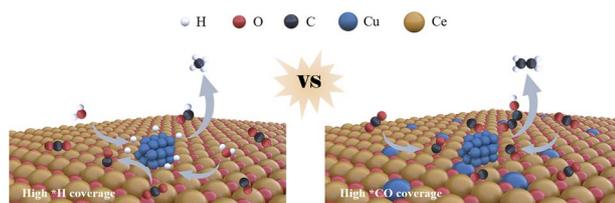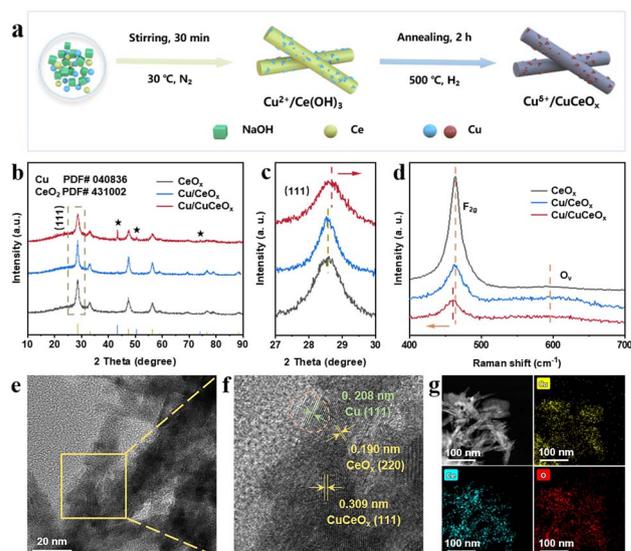


Fig. 2 (a) Synthetic route of the Cu/$CuCeO_x$ catalyst by a coprecipitation method. (b) XRD spectra, (c) local amplification of (111) and (d) Raman spectra for $CeO_x$, Cu/$CeO_x$, and Cu/$CuCeO_x$ catalysts ($CeO_2$, yellow, PDF# 43-1002; Cu, blue, PDF# 04-0836). (e and f) HRTEM images and (g) EDX elemental distribution mapping images of Cu/$CuCeO_x$.

coprecipitation; thereafter, Cu/$CeO_x$ was produced by an impregnation technique. The X-ray diffraction (XRD) analysis of the synthesized samples (Fig. 2b) reveals diffraction peaks at 28.55°, 32.08°, 47.48°, 56.34°, 59.09°, 69.42°, 76.70°, 79.08°, and 88.43°, congruent with the established cubic fluorite-like structure of $CeO_2$ (PDF# 43-1002). Additionally, characteristic diffraction peaks of Cu are discernible (indicated by a pentagram at 43.30°, 50.43°, and 74.13°) corresponding to PDF# 04-0836. Notably, the (111) plane of Cu/$CuCeO_x$ exhibits a discernible shift towards higher Bragg angles compared to $CeO_x$ and Cu/$CeO_x$ (Fig. 2c), suggesting the formation of a $Cu–Ce–O_x$ solid solution due to the substitution of a larger cation by a smaller one.[25–27] As the Cu content continues to increase, some of the copper precipitates out, forming clustered copper species on the Cu/$CuCeO_x$ nanorods.[28] And no diffraction peaks corresponding to Cu can be found when the copper loading is below 30 wt%, which may be due to the high dispersion of Cu nanoparticles with too small particle sizes on the surface of the ceria support to be identified by the XRD (Fig. S2†).[29,30] Raman spectroscopy of the catalysts reveals an intense band around 459 cm$^{-1}$ and another at approximately 595 cm$^{-1}$, corresponding to the $F_{2g}$ vibration pattern and defect-induced mode ($O_v$) in a cubic fluorite structure, respectively.[31] Notably, the $F_{2g}$ bands of Cu/$CuCeO_x$ exhibit a redshift to lower frequencies with increasing Cu loading, compared to pure $CeO_x$ (Fig. S3†), indicative of Cu atom doping into the $CeO_x$ lattice and Cu/$CuCeO_x$ interface formation.[32,33] This results in extended Ce–O bond lengths at the interface and lattice distortions due to the atomic radius disparity between $Cu^+$ and $Ce^{4+}$/$Ce^{3+}$,[34,35] corroborating the XRD findings.

Transmission electron microscopy (TEM, Fig. S4†) images depict the Cu/$CuCeO_x$ as possessing rod-like nanostructures.



Fig. 1 Diagrams of methane and ethylene production on Cu/$CeO_x$ and Cu/$CuCeO_x$ during the $CO_2RR$, respectively.

20116 | J. Mater. Chem. A, 2024, 12, 20115–20120

This journal is © The Royal Society of Chemistry 2024

The dynamic light scattering in Fig. S5† further illustrates that the particle size distribution between 50 and 200 nm is slightly wider than that presented by TEM, which may be caused by partial rupture or aggregation of cerium dioxide. High-resolution TEM (HRTEM) images (Fig. 2e and f) identify the main interplanar spacings of 0.309 nm corresponding to the Cu–Ce–O$_x$ (111), slightly smaller than the Cu/CeO$_x$'s CeO$_2$ (111) plane (0.312 nm) observed in Fig. S6.† Other characteristic $d$-spacings at 0.190 and 0.208 nm correspond to the CeO$_2$ (220) and Cu (111) planes, respectively. Elemental mapping *via* energy-dispersive X-ray spectroscopy (EDS, Fig. 2g) confirms the uniform distribution of Cu, Ce, and O within Cu/CuCeO$_x$ without significant agglomeration. Moreover, inductively coupled plasma atomic emission spectroscopy (ICP-OES) quantified the Ce and Cu composition, aligning closely with theoretical expectations (Table S1†).

The valence states and surface chemistry of Cu, Ce, and O were investigated by X-ray photoelectron spectroscopy (XPS). The Ce 3d XPS spectra for both Cu/CeO$_x$ and Cu/CuCeO$_x$ nanorods, depicted in Fig. 3a, were deconvoluted into eight peaks corresponding to Ce 3d$_{5/2}$ (v, 882.4 eV; v′,884.9 eV; v″, 888.7 eV; v‴, 898.2 eV) and Ce 3d$_{3/2}$ states (μ, 900.8 eV; μ′, 903.5 eV; μ″, 907.2 eV; μ‴, 916.6 eV).[36,37] Peaks designated v, v″, v‴, μ, μ″, and μ‴ are indicative of Ce$^{4+}$ species, while the v′ and μ′ peaks are attributed to Ce$^{3+}$ species, denoting the coexistence of Ce$^{4+}$ and Ce$^{3+}$ within the composite matrix.[38] The relative abundance of Ce$^{3+}$ to total cerium species was quantitatively assessed and was summarized in Table S1.† The ratio of Ce$^{3+}$ in Cu/CeO$_x$ and Cu/CuCeO$_x$ is 0.114 and 0.128, respectively. A noteworthy observation was the positive shift in the Ce$^{4+}$ peaks for Cu/CuCeO$_x$ (Fig. S7†), suggestive of alterations in the central charge distribution between Cu and Ce.[39] The Cu/CuCeO$_x$ exhibited a predominance of Ce$^{3+}$ species, which are postulated to facilitate rapid electron transport and mitigate electron localization at the Cu$^{2+}$/Cu$^+$ sites within the Cu–Ce–O$_x$ solid solution matrix.[40] The O 1s XPS spectra are analyzed in Fig. 3b,

which can be resolved into two distinct peaks by deconvolution: one at a lower binding energy of 529.3 eV associated with lattice oxygen (O$_{latt}$) and another at 531.3 eV, ascribed to adsorbed oxygen species (O$_{ads}$).[41] The number of oxygen vacancies calculated from the deconvoluted core level O 1s spectra is shown in Table S1.† The Cu 2p XPS spectra (Fig. 3c) exhibit binding energies of 952.7 eV and 932.9 eV, characteristic of Cu$^+$ or Cu$^0$ species.[42,43] A minor presence of CuO, attributed to inevitable surface oxidation, was also noted.[39,44] Given the challenges in distinguishing between Cu$^0$ and Cu$^+$ based on Cu 2p$_{3/2}$ spectra alone,[29] additional analysis was conducted using Cu LMM Auger kinetic energy spectra (Fig. 3d), where peaks at 570.0 and 565.3 eV substantiate the presence of Cu$^+$ and Cu$^0$ species, respectively.[45,46] Herein, most of the Cu on the surface is oxidized to monovalent Cu species. The Cu/CuCeO$_x$ sample possesses the most surface monovalent Cu species (0.78), much higher than that of Cu/CeO$_x$ (0.56). The presence of monovalent copper is conducive to the adsorption of *CO.[47]

The CO$_2$RR catalytic performances of Cu/CuCeO$_x$ catalysts were tested in a flow cell, in which 1.0 M KOH was used as the electrolyte. In this work, all the applied potentials were converted into a reversible hydrogen electrode (RHE) scale without *iR* correction. The linear sweep voltammetry curves (LSV) shown in Fig. 4a were recorded by feeding the CO$_2$ gas across the 1.0 M KOH interface. Note that the Cu/CuCeO$_x$ catalysts exhibited higher current density responses than those of CeO$_x$ and Cu/CeO$_x$ catalysts, and we assume that the formation of Cu–Ce–O$_x$ solid solutions may enrich active sites that kinetically favored the CO$_2$RR. To verify the hypothesis, we conducted the cyclic voltammetry (CV) method to estimate the electrochemically active surface area (ECSA) of the catalysts (Fig. S8†). The results show that Cu/CuCeO$_x$ had larger ECSA values than the Cu/CeO$_x$ catalyst, indicating that the generation of Cu–Ce–O$_x$ solid
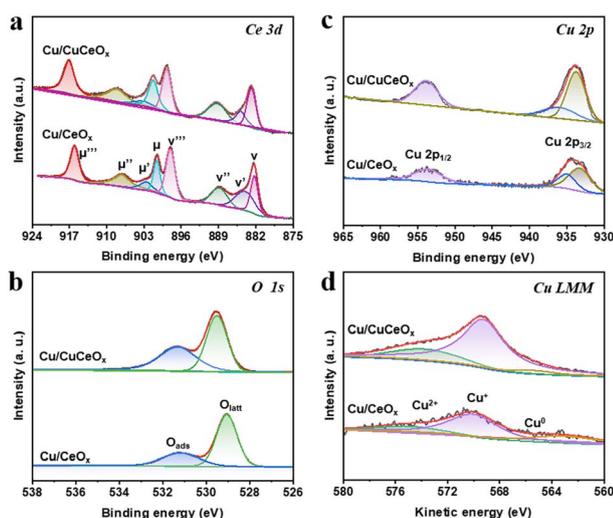
**Fig. 3** XPS analysis of (a) Ce 3d, (b) O 1s, (c) Cu 2p, and (d) Cu LMM Auger spectra for Cu/CeO$_x$ and Cu/CuCeO$_x$.
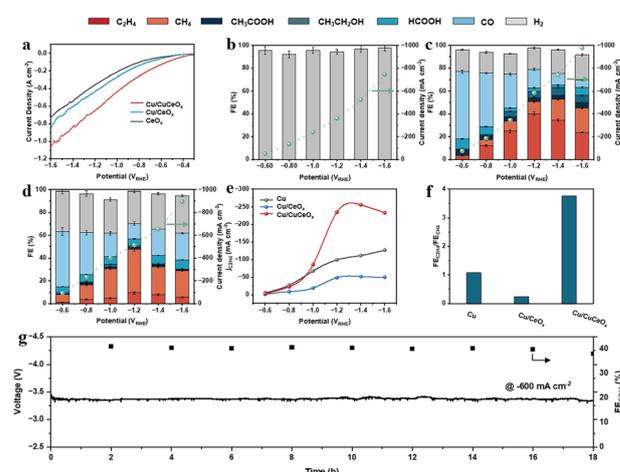
**Fig. 4** (a) LSV spectra of CeO$_x$, Cu/CeO$_x$, and Cu/CuCeO$_x$ catalysts. (b–d) FEs of products at different applied potentials in 1.0 M KOH electrolyte for CeO$_x$, Cu/CuCeO$_x$, and Cu/CeO$_x$. (e) C$_2$H$_4$ partial current densities of Cu, Cu/CeO$_x$ and Cu/CuCeO$_x$ under different potentials. (f) FE$_{C_2H_4}$/FE$_{CH_4}$ of CeO$_x$, Cu/CeO$_x$, and Cu/CuCeO$_x$ at −1.2 V$_{RHE}$. (g) Stability test of Cu/CuCeO$_x$ during 18 h of long-time operation at −600 mA cm$^{-2}$.

This journal is © The Royal Society of Chemistry 2024

*J. Mater. Chem. A*, 2024, **12**, 20115–20120 | **20117**

solutions favors the kinetics of the $CO_2RR$ *via* generating more interfacial active sites, which is consistent with the results of impedance analysis (Fig. S9†).

The gaseous and liquid products were quantitatively analyzed by on-line gas chromatography (GC, Fig. S10†) and $^1H$ nuclear magnetic resonance ($^1H$ NMR, Fig. S11†), respectively.[48] For the pure $CeO_2$ catalyst, $H_2$ was the main product (Fig. 4b). As shown in Fig. 4c, the $Cu/CuCeO_x$ catalyst exhibited a high $FE_{C_2H_4}$ of 40.2% at $-1.2$ $V_{RHE}$. In comparison, the Cu and $Cu/CeO_x$ catalysts showed lower $FE_{C_2H_4}$ at $-1.2$ $V_{RHE}$ (Fig. 4d and S12†). For the pure Cu catalyst, the major products were $H_2$, $CH_4$, and $C_2H_4$ species, while $FE_{CH_4}$ and $FE_{C_2H_4}$ were 18.9% and 20.5%, respectively (Fig. S12†). In contrast, for the $Cu/CeO_x$ catalyst, $CH_4$ emerged as the predominant product, achieving a FE of 38.6% at a potential of $-1.2$ $V_{RHE}$. The comparison of FE for $H_2$ and the $CH_4$ products over those three catalysts further demonstrated that the formation of $H_2$ and the $CH_4$ species was suppressed on the $Cu/CuCeO_x$ catalyst. Furthermore, LSV measurements in an Ar-saturated 1.0 M KOH electrolyte without $CO_2$ gas revealed that $CeO_x$ exhibited the lowest overpotential at equivalent current densities, further affirming its proficiency in hydrogen evolution (Fig. S13†). Furthermore, the $Cu/CuCeO_x$ catalyst demonstrated the highest partial current density for $C_2H_4$ production (Fig. 4e), signifying that $Cu/CuCeO_x$ has superior catalytic activity for $C_2H_4$ synthesis compared to both pristine Cu and $Cu/CeO_x$. Fig. 4f illustrates that the $FE_{C_2H_4}/FE_{CH_4}$ ratio achieved a maximum of 3.77 on $Cu/CuCeO_x$, compared to 1.08 and 0.25 for Cu and $Cu/CeO_x$, respectively, indicating that the formation of $Cu–Ce–O_x$ solid solutions is particularly conducive to $C_2H_4$ production. Comparative electrochemical evaluations of $Cu_{0.1}/CuCeO_x$ and $Cu_{0.5}/CuCeO_x$, synthesized *via* the same method, were also performed (Fig. S14†). A 50% increase in Cu loading led to a decline in $C_2H_4$ selectivity, potentially due to the formation of larger Cu particles, which diminish the number of Cu active sites directly interacting with Ce, thereby inhibiting C–C coupling.[36] The long-term stability of $Cu/CuCeO_x$ was assessed through chronopotentiometry, and no significant decrease in Faraday efficiency of $C_2H_4$ was observed during 18 h of electrocatalysis at $-600$ mA cm$^{-2}$ (Fig. 4g). Post-$CO_2RR$ XPS analysis of the electrode confirmed the persistence of Cu$^+$ as the predominant valence state in $Cu/CuCeO_x$, indirectly evidencing the stabilizing influence of the $Cu–Ce–O_x$ matrix on Cu$^+$ species (Fig. S15 and Table S1†). The efficient presence of Cu$^+$ was also demonstrated by *in situ* Raman spectra of a wide potential window (Fig. S16†), with characteristic peaks around 150, 230 and 500 cm$^{-1}$.[49,50] Moreover, the characteristic peaks of the *CO (2050 cm$^{-1}$) intermediates were also observed, further indicating the high *CO concentration on the $Cu/CuCeO_x$ catalyst surface.

Subsequent density functional theory (DFT) calculations were conducted for $Cu/CeO_x$ and $Cu/CuCeO_x$ catalysts to rationalize the effects of $Cu–Ce–O_x$ solid solutions on the $CO_2RR$ selectivity toward $C_2H_4$ (Experimental section in the ESI, Fig. S17 and S18†). Initially, Bader charge analysis was applied to $Cu/CuCeO_x$ (Fig. 5a), revealing that copper integration into the cerium dioxide matrix diminished the charge density around the Cu sites, indicating that the charges of Cu and Ce were
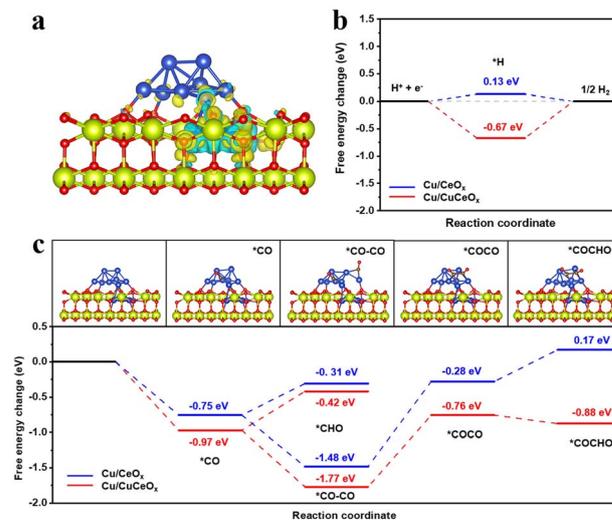


Fig. 5 (a) The Bader charge of $Cu/CuCeO_x$. (b) Desorption energy diagram of hydrogen on $Cu/CeO_x$ and $Cu/CuCeO_x$. (c) The free energy change diagram of *CHO or *COCHO generated by *CO over the $Cu/CeO_x$ and $Cu/CuCeO_x$.

rearranged.[51] The transfer of electrons from Cu to Ce$^{3+}$ results in higher Cu$^+$ in $Cu/CuCeO_x$, which is conducive to promoting the adsorption of *CO on the surface and enhancing C–C to achieve high selectivity of $C_2H_4$. This alteration favorably impacts the protonation of *COCO intermediates, thereby facilitating $C_2H_4$ formation. In addition, the hydrogen evolution reaction (HER) performance of both $Cu/CeO_x$ and $Cu/CeCuO_x$ was assessed (Fig. 5b). The Gibbs free energy ($|\Delta G_{H^*}|$) for the HER on $Cu/CeO_x$ is 0.13 eV lower than that of $Cu/CeCuO_x$ (0.67 eV), thus allowing the promotion of the surface *H coverage and the hydrogenation.

The free energy diagrams depicting the formation of *CHO or *COCHO from *CO on the $Cu/CeO_x$ or $Cu/CuCeO_x$ catalysts are presented in Fig. 5c. Moreover, $Cu/CuCeO_x$ also exhibits significantly stronger *CO adsorption than $Cu/CuO_x$, enhancing the local *CO concentration and favoring the C–C coupling process on the $Cu/CeCuO_x$ catalyst. According to previous reports,[52] the formation of $CH_4$ and $C_2H_4$ is primarily governed by distinct rate-determining steps: the hydrogenation of *CO to *CHO for $CH_4$, and the coupling of *CO with *CHO for $C_2H_4$, respectively.[20,53] For the $Cu/CeO_x$ catalyst, the $\Delta G$ value of the CO hydrogenation is 0.44 eV lower than that of the $Cu/CeCuO_x$ catalyst, suggesting that $Cu/CeO_x$ has a higher selectivity for producing $CH_4$. In contrast, the formation of the *COCHO intermediate of the $Cu/CuCeO_x$ catalyst (0.12 eV) requires less free energy change than that of the $Cu/CuO_x$ catalyst (0.45 eV), indicating a more favorable $C_2H_4$ pathway. Our computational findings corroborated that surfaces characterized by relatively high *H and low *CO coverage are conducive to the promotion of $CH_4$ production. Conversely, surfaces with a rich presence of *CO and moderate levels of *H are advantageous for the synthesis of $C_2H_4$.

Lastly, *in situ* infrared spectroscopy was employed to analyze potential surface intermediates on $Cu/CeO_x$ and $Cu/CuCeO_x$

**20118** | *J. Mater. Chem. A*, 2024, **12**, 20115–20120

This journal is © The Royal Society of Chemistry 2024

under various potential conditions, further elucidating the catalytic mechanism (Fig. S19†). Not only the peak of $CO_2$ can be observed in a pronounced absorption band of 2400–2300 cm$^{-1}$,[54,55] but also the characteristic peak of CO (2050 cm$^{-1}$) can also be identified,[56] which serves as evidence for the activation and reduction of $CO_2$.[57] In addition, a distinct *CHO peak, key intermediate for $CH_4$, was further found at 1226 cm$^{-1}$.[58] In contrast, in the Cu/CuCeO$_x$ spectrum, the characteristic peak of *CHO is significantly weakened and replaced by *COCHO at 1550 and 1185 cm$^{-1}$,[59–62] indicating that Cu/CuCeO$_x$ catalysts are more inclined to produce $C_2$, which is consistent with the results calculated by DFT.

## Conclusions

In summary, this study successfully demonstrates the selective electroreduction of $CO_2$ to $CH_4$ or $C_2H_4$ by finely tuning *H and *CO adsorption on Cu/CeO$_x$ catalysts. Our innovative approach, involving the manipulation of Cu/CeO$_x$ and Cu/CuCeO$_x$ interfaces, significantly influences the catalytic selectivity towards desired $C_1$ or $C_2$ products. Notably, the Cu/CuCeO$_x$ electrocatalyst demonstrated a peak FE$_{C_2H_4}$ of 40.2% and $j_{C_2H_4}$ of −245.7 mA cm$^{-2}$, while the Cu/CeO$_x$ electrocatalyst showed good $CO_2$RR performances with a maximum FE$_{CH_4}$ of 38.6% and $j_{CH_4}$ of −198.3 mA cm$^{-2}$. This advancement is underpinned by the enhanced *CO adsorption facilitated by the stabilization of Cu$^+$ species within the Cu–Ce–O$_x$ solid solution. Our findings pave the way for the development of tailored catalysts capable of directing $CO_2$ electroreduction towards specific hydrocarbons, addressing critical needs in $CO_2$ mitigation and sustainable fuel production.

## Data availability

All the data supporting this article have been included in the main text and the ESI.†

## Author contributions

M. K. proposed, designed, and supervised the project. T. H., Y. B., Z. C., and J. P. wrote the manuscript. T. H., Y. B., and Z. C. performed the experiments and analyzed the data. All authors discussed the results and revised the manuscript.

## Conflicts of interest

The authors declare no conflicts of interest.

## Acknowledgements

## References

1 M. Li, F. Zhang, M. Kuang, Y. Ma, T. Liao, Z. Sun, W. Luo, W. Jiang and J. Yang, *Nano-Micro Lett.*, 2023, **15**, 238.

2 M. B. Ross, P. De Luna, Y. Li, C.-T. Dinh, D. Kim, P. Yang and E. H. Sargent, *Nat. Catal.*, 2019, **2**, 648.

3 Y. Ma, J. Wang, J. Yu, J. Zhou, X. Zhou, H. Li, Z. He, H. Long, Y. Wang, P. Lu, J. Yin, H. Sun, Z. Zhang and Z. Fan, *Matter*, 2021, **4**, 888.

4 W. Ma, S. Xie, T. Liu, Q. Fan, J. Ye, F. Sun, Z. Jiang, Q. Zhang, J. Cheng and Y. Wang, *Nat. Catal.*, 2020, **3**, 478.

5 H. Chen, Z. Wang, X. Wei, S. Liu, P. Guo, P. Han, H. Wang, J. Zhang, X. Lu and B. Wei, *Appl. Surf. Sci.*, 2021, **544**, 148965.

6 W. Ma, S. Xie, X.-G. Zhang, F. Sun, J. Kang, Z. Jiang, Q. Zhang, D.-Y. Wu and Y. Wang, *Nat. Commun.*, 2019, **10**, 892.

7 W. Zhu, L. Fan, Q. Geng, C. Wang, X. Fan, Y. Zhang and C. Li, *Chem. Eng. J.*, 2024, **489**, 151316.

8 S. Jin, Z. Hao, K. Zhang, Z. Yan and J. Chen, *Angew. Chem., Int. Ed.*, 2021, **60**, 20627–20648.

9 Q.-J. Wu, D.-H. Si, P.-P. Sun, Y.-L. Dong, S. Zheng, Q. Chen, S.-H. Ye, D. Sun, R. Cao and Y.-B. Huang, *Angew. Chem., Int. Ed.*, 2023, **62**, e202306822.

10 J. Zhang, C. Guo, S. Fang, X. Zhao, L. Li, H. Jiang, Z. Liu, Z. Fan, W. Xu, J. Xiao and M. Zhong, *Nat. Commun.*, 2023, **14**, 1298.

11 Z. Zhang, L. Bian, H. Tian, Y. Liu, Y. Bando, Y. Yamauchi and Z.-L. Wang, *Small*, 2022, **18**, 2107450.

12 H. Shi, L. Luo, C. Li, Y. Li, T. Zhang, Z. Liu, J. Cui, L. Gu, L. Zhang, Y. Hu, H. Li and C. Li, *Adv. Funct. Mater.*, 2024, **34**, 2310913.

13 Y. Sun, J. Xie, Z. Fu, H. Zhang, Y. Yao, Y. Zhou, X. Wang, S. Wang, X. Gao, Z. Tang, S. Li, X. Wang, K. Nie, Z. Yang and Y.-M. Yan, *ACS Nano*, 2023, **17**, 13974.

14 L. Ma, Q. Geng, L. Fan, J.-X. Li, D. Du, J. Bai and C. Li, *Nano Res.*, 2023, **16**, 9065–9072.

15 X. Xie, X. Zhang, M. Xie, L. Xiong, H. Sun, Y. Lu, Q. Mu, M. H. Rummeli, J. Xu, S. Li, J. Zhong, Z. Deng, B. Ma, T. Cheng, W. A. Goddard and Y. Peng, *Nat. Commun.*, 2022, **13**, 63.

16 T. Yan, P. Wang and W.-Y. Sun, *Small*, 2023, **19**, 2206070.

17 Q. Bie, H. Yin, Y. Wang, H. Su, Y. Peng and J. Li, *Chin. J. Catal.*, 2024, **57**, 96.

18 T. Zheng, C. Liu, C. Guo, M. Zhang, X. Li, Q. Jiang, W. Xue, H. Li, A. Li, C.-W. Pao, J. Xiao, C. Xia and J. Zeng, *Nat. Nanotechnol.*, 2021, **16**, 1386.

19 C. Chen, S. Yu, Y. Yang, S. Louisia, I. Roh, J. Jin, S. Chen, P.-C. Chen, Y. Shan and P. Yang, *Nat. Catal.*, 2022, **5**, 878.

20 J. Feng, L. Zhang, S. Liu, L. Xu, X. Ma, X. Tan, L. Wu, Q. Qian, T. Wu, J. Zhang, X. Sun and B. Han, *Nat. Commun.*, 2023, **14**, 4615.

21 Y. Chen, N. Lyu, J. Zhang, S. Yan, C. Peng, C. Yang, X. Lv, C. Hu, M. Kuang and G. Zheng, *Small*, 2024, 2308004.

22 X. Wang, A. Xu, F. Li, S.-F. Hung, D.-H. Nam, C. M. Gabardo, Z. Wang, Y. Xu, A. Ozden, A. S. Rasouli, A. H. Ip, D. Sinton and E. H. Sargent, *J. Am. Chem. Soc.*, 2020, **142**, 3525.

23 Q. Zhao, J. M. P. Martirez and E. A. Carter, *J. Am. Chem. Soc.*, 2021, **143**, 6152.

This journal is © The Royal Society of Chemistry 2024

*J. Mater. Chem. A*, 2024, **12**, 20115–20120 | **20119**

24 X. Guo, W. Ye, Z. a. Chen, A. Zhou, D. Jin and T. Ma, *Appl. Catal., B*, 2022, **310**, 121334.

25 W. Shan, W. Shen and C. Li, *Chem. Mater.*, 2003, **15**, 4761.

26 W. Liu, X. Liu, L. Feng, J. Guo, A. Xie, S. Wang, J. Zhang and Y. Yang, *Nanoscale*, 2014, **6**, 10693.

27 C.-A. Thieu, S. Yang, H.-I. Ji, H. Kim, K. J. Yoon, J.-H. Lee and J.-W. Son, *J. Mater. Chem. A*, 2022, **10**, 2460.

28 J. Jiang, H. Yang, H. Jiang, Y. Hu and C. Li, *Chem. Eng. J.*, 2023, **471**, 144439.

29 C. He, Y. Yu, L. Yue, N. Qiao, J. Li, Q. Shen, W. Yu, J. Chen and Z. Hao, *Appl. Catal., B*, 2014, **147**, 156.

30 P. Bera, K. R. Priolkar, P. R. Sarode, M. S. Hegde, S. Emura, R. Kumashiro and N. P. Lalla, *Chem. Mater.*, 2002, **14**, 3591.

31 B. Levasseur, A. M. Ebrahim and T. J. Bandosz, *Langmuir*, 2011, **27**, 9379.

32 T. Masui, K. Koyabu, K. Minami, T. Egawa and N. Imanaka, *J. Phys. Chem. C*, 2007, **111**, 13892.

33 S. Zhang, B. Jiang, M. Tong, Y. Yang, Z. Liao, Z. Huang, J. Sun, J. Wang and Y. Yang, *Ind. Eng. Chem. Res.*, 2023, **62**, 20667.

34 F. Jiang, S. Wang, B. Liu, J. Liu, L. Wang, Y. Xiao, Y. Xu and X. Liu, *ACS Catal.*, 2020, **10**, 11493.

35 H. Sun, H. Wang and Z. Qu, *ACS Catal.*, 2023, **13**, 1077.

36 S. Jin, D. Li, Z. Wang, Y. Wang, L. Sun and M. Zhu, *Catal. Sci. Technol.*, 2022, **12**, 7003.

37 M. Yusufoğlu, S. Tafazoli, H. Jahangiri, M. B. Yağcı, T. Balkan and S. Kaya, *ACS Appl. Mater. Interfaces*, 2024, **16**, 7288.

38 C. W. Lee, S.-J. Shin, H. Jung, D. L. T. Nguyen, S. Y. Lee, W. H. Lee, D. H. Won, M. G. Kim, H.-S. Oh, T. Jang, H. Kim, B. K. Min and Y. J. Hwang, *ACS Energy Lett.*, 2019, **4**, 2241.

39 G. Tang, Y. Wu, J. Zhao, H. Zhang, M. Zhou and Y. Wang, *Chem.–Eur. J.*, 2022, **28**, e202103459.

40 Z. Yang, D. Ji, Z. Li, Z. He, Y. Hu, J. Yin, Y. Hou, P. Xi and C.-H. Yan, *Small*, 2023, **19**, 2303099.

41 W. Wang, Q. Zhu, F. Qin, Q. Dai and X. Wang, *Chem. Eng. J.*, 2018, **333**, 226.

42 R. Feng, Q. Zhu, M. Chu, S. Jia, J. Zhai, H. Wu, P. Wu and B. Han, *Green Chem.*, 2020, **22**, 7560.

43 J. Shan, Y. Shi, H. Li, Z. Chen, c. Sun, Y. Shuai and Z. Wang, *Chem. Eng. J.*, 2022, **433**, 133769.

44 K. Cao, H. Liu, W. Li, Q. Han, Z. Zhang, K. Huang, Q. Jing and L. Jiao, *Small*, 2019, **15**, 1901775.

45 S. Y. Lee, H. Jung, N.-K. Kim, H.-S. Oh, B. K. Min and Y. J. Hwang, *J. Am. Chem. Soc.*, 2018, **140**, 8681.

46 N. Martić, C. Reller, C. Macauley, M. Löffler, B. Schmid, D. Reinisch, E. Volkova, A. Maltenberger, A. Rucki, K. J. J. Mayrhofer and G. Schmid, *Adv. Energy Mater.*, 2019, **9**, 1901228.

47 B. Yang, W. Deng, L. Guo and T. Ishihara, *Chin. J. Catal.*, 2020, **41**, 1348–1359.

48 S. Liu, Y. Cao, H. Liu, H. Wang, B. Zhang, Y. Zhang, L. Zhang, S. Zhang and J. Sun, *Nanoscale*, 2021, **13**, 16986.

49 A. Xu, S.-F. Hung, A. Cao, Z. Wang, N. Karmodak, J. E. Huang, Y. Yan, A. Sedighian Rasouli, A. Ozden, F.-Y. Wu, Z.-Y. Lin, H.-J. Tsai, T.-J. Lee, F. Li, M. Luo, Y. Wang, X. Wang, J. Abed, Z. Wang, D.-H. Nam, Y. C. Li, A. H. Ip, D. Sinton, C. Dong and E. H. Sargent, *Nat. Catal.*, 2022, **5**, 1081–1088.

50 M. Wang, Z. Wang, Z. Huang, M. Fang, Y. Zhu and L. Jiang, *ACS Nano*, 2024, **18**, 15303–15311.

51 J. Zhang, P. Yu, C. Peng, X. Lv, Z. Liu, T. Cheng and G. Zheng, *ACS Catal.*, 2023, **13**, 7170.

52 L. Xiong, X. Zhang, L. Chen, Z. Deng, S. Han, Y. Chen, J. Zhong, H. Sun, Y. Lian, B. Yang, X. Yuan, H. Yu, Y. Liu, X. Yang, J. Guo, M. H. Rümmeli, Y. Jiao and Y. Peng, *Adv. Mater.*, 2021, **33**, 2101741.

53 A. Vasileff, C. Xu, Y. Jiao, Y. Zheng and S. Z. Qiao, *Chem*, 2018, **4**, 1809.

54 G. N. Vayssilov, M. Mihaylov, P. S. Petkov, K. I. Hadjiivanov and K. M. Neyman, *J. Phys. Chem. C*, 2011, **115**, 23435.

55 Y. Yan, R. J. Wong, Z. Ma, F. Donat, S. Xi, S. Saqline, Q. Fan, Y. Du, A. Borgna, Q. He, C. R. Müller, W. Chen, A. A. Lapkin and W. Liu, *Appl. Catal., B*, 2022, **306**, 121098.

56 J. Yin, Z. Gao, F. Wei, C. Liu, J. Gong, J. Li, W. Li, L. Xiao, G. Wang, J. Lu and L. Zhuang, *ACS Catal.*, 2022, **12**, 1004.

57 Y. Katayama, F. Nattino, L. Giordano, J. Hwang, R. R. Rao, O. Andreussi, N. Marzari and Y. Shao-Horn, *J. Phys. Chem. C*, 2019, **123**, 5951.

58 P. Wang, H. Yang, C. Tang, Y. Wu, Y. Zheng, T. Cheng, K. Davey, X. Huang and S.-Z. Qiao, *Nat. Commun.*, 2022, **13**, 3754.

59 L. Zhang, J. Feng, L. Wu, X. Ma, X. Song, S. Jia, X. Tan, X. Jin, Q. Zhu, X. Kang, J. Ma, Q. Qian, L. Zheng, X. Sun and B. Han, *J. Am. Chem. Soc.*, 2023, **145**, 21945.

60 Q. Geng, L. Fan, H. Chen, C. Zhang, Z. Xu, Y. Tian, C. Yu, L. Kang, Y. Yamauchi, C. Li and L. Jiang, *J. Am. Chem. Soc.*, 2024, **146**, 10599–10607.

61 L. Fan, Q. Geng, L. Ma, C. Wang, J.-X. Li, W. Zhu, R. Shao, W. Li, X. Feng, Y. Yamauchi, C. Li and L. Jiang, *Chem. Sci.*, 2023, **14**, 13851–13859.

62 S. Hu, Y. Chen, Z. Zhang, S. Li, H. Liu, X. Kang, J. Liu, S. Ge, J. Wang, W. Lv, Z. Zeng, X. Zou, Q. Yu and B. Liu, *Small*, 2024, **20**, 2308226.

**20120** | *J. Mater. Chem. A*, 2024, **12**, 20115–20120

This journal is © The Royal Society of Chemistry 2024